Journal of Engineering Mathematics **35:** 85–107, 1999.

Waves generated by a moving source in a two-layer ocean of finite depth

R. W. YEUNG* and T. C. NGUYEN**
Department of Mechanical Engineering and Ocean Engineering Graduate Group, University of California at Berkeley, Berkeley CA 94720-1740, U.S.A.
***Present address: Coastal Systems Station, Department of the Navy, Panama City, FL 32407-7001, USA.*

Received 27 July 1997; accepted in final form 3 February 1998

Abstract. The velocity potentials of a point source moving at a constant velocity in the upper layer of a two-layer fluid are obtained in a form amenable to numerical integration. Each fluid layer is of finite depth, and the density difference between the two layers is not necessarily small. The far-field asymptotic behavior of the surface waves and internal waves are also derived using the method of stationary phase. They show that the wave system at the free surface or at the interface each contains contributions from two different modes: a surface-wave mode and an internal-wave mode. When the density difference between the two layers is small or the depth of the upper layer is large, the surface-wave mode mainly affects the surface waves while the internal-wave mode mainly affects the internal waves. However, for large density difference, both modes contribute to the surface wave or internal wave system. For each mode, both divergent and transverse waves are present if the total depth Froude number is less than a certain critical Froude number which is mode-dependent. For depth Froude number greater than the critical Froude number, only divergent waves exist for that mode. This classification is similar to that of a uniform fluid of finite depth, where the critical Froude number is simply unity. The surface waves and internal waves are also calculated using the full expressions of the source potentials. They further confirm and illustrate the features observed in the asymptotic analysis.

Keywords: gravity waves, internal waves, stratified flow, Green's function, shallow-water effects, Froude number, wave patterns, asymptotics

1. Introduction

Density stratification is a common occurrence in the ocean owing to variation of water temperature and salinity with depth. Very often the density gradient occurs within a thin pycnocline separating two well-mixed fluid layers of almost constant density. This pycnocline structure can be modeled by a two-layer fluid with a density jump across the interface. In this model, the fluid in each layer is assumed to be inviscid, incompressible and have a constant density.

Surface or sub-surface marine vehicles sometimes operate in such a stratified environment and can generate both surface and internal waves. This generation of internal waves gives rise to some interesting hydrodynamic phenomena, such as the 'dead-water' effect (Ekman [1], Miloh *et al.* [2, 3]) and possibly the narrow V wakes observed in synthetic aperture radar (SAR) images (Hughes [4], Tulin and Miloh [5]). Also of intrinsic interest are the wave patterns created on the free surface and on the interface. They are important with regard to the visual detectability of sub-surface vehicles. Theoretical investigations of the internal-wave patterns have been carried out by various authors. The far-field kinematical wave patterns were obtained by Keller and Munk [6] using ray methods and also by Yih [7], Tulin and Miloh [5]

* Correspondence author, e-mail: rwyeung@socrates.berkeley.edu.

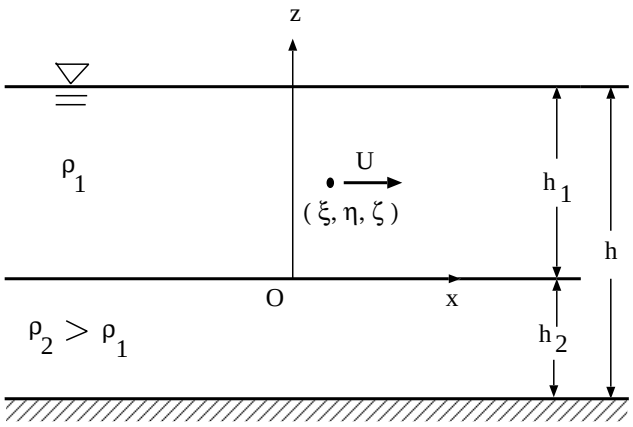

Figure 1. Definition of coordinate system.

using equivalent asymptotics. For the highly supercritical case, where the speed of the ship is much greater than the phase speed of the internal waves, the internal-wave wakes are then very narrow, and numerical cross-flow theories have been used to compute the internal waves (Tulin, Wang, and Yao [8], Wong and Calisal [9]). Earlier, Yeung and Kim [10] pointed out that such cross-flow theory can only capture the presence of divergent waves. Other works on this subject deal with the Green functions for a two-layer fluid. Hudimac [11] derived the Green functions for an infinitely deep lower fluid layer. He showed the internal wave crests in the far field for both the subcritical and supercritical case. Crapper [12] extended the study to a pressure point and introduced a less cumbersome method for dealing with the asymptotics. Other works on Green functions in a two-layer fluid include those of Sretenskii [13], Uspenskii [14], and Sabunçu [15]. These authors focused on the internal-wave resistance of thin ships of the Michell type [16]. Uspenskii [14] assumed the fluid to be of finite depth, and Sabunçu [15] considered other cases where the upper fluid is either infinitely thick or bounded by a rigid surface. More recently, in addressing the 'dead-water' problem, Miloh *et al.* [3] derived the Green functions for a two-layer fluid of finite depth and also showed some results for the internal waves in the case of small density difference between the two fluid layers.

In the above mentioned studies on wave patterns in a two-layer fluid, attentions were usually focused on the internal waves. If the density difference between the two fluid layers is small, the critical Froude number Fr_2, the Froude number corresponding to the fastest internal waves, is also small, and it would be reasonable to neglect the effects of the free surface. However, in the supersonic case, where the source Froude number is much greater than Fr_2, significant surface waves can be generated so that their effects on the internal wave pattern may not be negligible. Also, when large density difference exists, it is possible to generate significant disturbances on both the free surface and the interface, and interactions between the two wave systems may result in unsual surface and internal wave patterns.

In this paper, we derive the Green functions for a two-layer fluid of finite depth and use them to investigate the wave patterns on both the free surface and interface, with the fluid-depth ratio and density ratio being arbitrary. In such an approach, we are thus able to investigate in a unifying way how the two wave systems are coupled and their dependence on the said physical parameters.

2. Problem formulation

Consider a rectangular coordinate system moving with a source at a constant velocity U as shown in Figure 1. The x, y plane of this system coincides with the undisturbed interface between the two fluid layers. The positive x-axis points in the direction of motion of the source, and the positive z-axis points upward. The source is restricted to the upper fluid layer, and its location is denoted by (ξ, η, ζ). The densities and depths of the upper and lower fluid layer are indicated by ρ_1, h_1 and ρ_2, h_2, respectively.

As in Lamb [17], a fictitious dissipative force proportional to the perturbation velocity is introduced where the positive proportionality constant is denoted by μ. This force does not disturb the irrotational nature of the flow, but it does facilitate the satisfaction of the radiation condition and will be made zero in the final results. If the velocity potentials in the two fluid layers are denoted by $G^{(m)}(x, y, z)$, where $m = 1, 2$ refer to the upper and lower fluid layer, respectively, then the governing equations for $G^{(m)}(x, y, z)$ can be written as

$$\nabla^2 G^{(1)} = \delta(x - \xi, y - \eta, z - \zeta) \quad \text{and} \quad \nabla^2 G^{(2)} = 0, \tag{1}$$

where δ is the delta function. The linearized boundary conditions on the free surface and the interface are (see Sabunçu [15])

$$k_o G_z^{(1)} + G_{xx}^{(1)} - \mu G_x^{(1)} = 0, \quad z = h_1, \tag{2}$$

$$\gamma(k_o G_z^{(1)} + G_{xx}^{(1)} - \mu G_x^{(1)}) = k_o G_z^{(2)} + G_{xx}^{(2)} - \mu G_x^{(2)}, \quad z = 0, \tag{3}$$

$$G_z^{(1)} = G_z^{(2)}, \quad z = 0, \tag{4}$$

where $k_o = g/U^2$ and $\gamma = \rho_1/\rho_2$. Equation (2) is the usual mixed free-surface condition, whereas (3) and (4) are the dynamic and kinematic conditions on the interface. On the rigid bottom, the boundary condition is

$$G_z^{(2)} = 0, \qquad z = -h_2. \tag{5}$$

And finally, far upstream of the source, the fluid velocities must vanish.

$$\lim_{x \to \infty} \nabla G^{(m)} = 0. \tag{6}$$

3. Derivation of the Green functions

3.1. Fourier transforms

We assume the solutions $G^{(m)}$ to have the following forms:

$$G^{(1)} = \frac{1}{\tilde{r}} + G_o^{(1)} \quad \text{and} \quad G^{(2)} = G_o^{(2)}, \tag{7}$$

where $\tilde{r}^2 = (x - \xi)^2 + (y - \eta)^2 + (z - \zeta)^2$. The unknown functions $G_o^{(m)}$ must now satisfy the Laplace equation:

$$\nabla^2 G_o^{(m)} = 0. \tag{8}$$

To solve for $G^{(m)}$, we first introduce the following Fourier-transform pairs:

$$\begin{aligned} \mathcal{G}(k_1, k_2, z) &= \mathcal{F}\{G(x, y, z)\} \\ &\equiv \frac{1}{2\pi}\int_{-\infty}^{\infty}\int_{-\infty}^{\infty} G(x, y, z)\, \mathrm{e}^{-i[k_1(x-\xi)+k_2(y-\eta)]}\, \mathrm{d}x\, \mathrm{d}y, \end{aligned} \tag{9}$$

$$\begin{aligned} G(x, y, z) &= \mathcal{F}^{-1}\{\mathcal{G}(k_1, k_2, z)\} \\ &\equiv \frac{1}{2\pi}\int_{-\infty}^{\infty}\int_{-\infty}^{\infty} \mathcal{G}(k_1, k_2, z)\, \mathrm{e}^{i[k_1(x-\xi)+k_2(y-\eta)]}\, \mathrm{d}k_1\, \mathrm{d}k_2. \end{aligned} \tag{10}$$

The transform of Equation (8) becomes

$$\mathcal{G}_{o,zz}^{(m)} - (k_1^2 + k_2^2)\mathcal{G}_o^{(m)} = 0 \tag{11}$$

which has the following solution

$$\mathcal{G}_o^{(m)}(k_1, k_2, z) = A^{(m)}(k_1, k_2)\, \mathrm{e}^{kz} + B^{(m)}(k_1, k_2)\, \mathrm{e}^{-kz}, \tag{12}$$

where $k^2 = k_1^2 + k_2^2$. The Fourier transforms of the boundary conditions in Equations (2–5) are

$$k_o\mathcal{G}_z^{(1)} - k_1^2\mathcal{G}^{(1)} - i\mu k_1\mathcal{G}^{(1)} = 0, \quad z = h_1, \tag{13}$$

$$\gamma(k_o\mathcal{G}_z^{(1)} - k_1^2\mathcal{G}^{(1)} - i\mu k_1\mathcal{G}^{(1)}) = k_o\mathcal{G}_z^{(2)} - k_1^2\mathcal{G}^{(2)} - i\mu k_1\mathcal{G}^{(2)}, \quad z = 0, \tag{14}$$

$$\mathcal{G}_z^{(1)} = \mathcal{G}_z^{(2)}, \quad z = 0, \tag{15}$$

$$\mathcal{G}_z^{(2)} = 0, \quad z = -h_2. \tag{16}$$

Here $\mathcal{G}^{(1)} = \mathcal{F}\{G^{(1)}\} = \mathcal{F}\{1/r\} + \mathcal{G}_o^{(1)}$ and $\mathcal{G}^{(2)} = \mathcal{F}\{G^{(2)}\} = \mathcal{G}_o^{(2)}$. Substituting the following well-known relation (see Gradshteyn and Ryzhik [18])

$$\mathcal{F}\left\{\frac{1}{r}\right\} = \frac{\mathrm{e}^{-k|z-\zeta|}}{k} \tag{17}$$

and Equation (12) into the above boundary conditions, we obtain a system of linear equations for the four unknown coefficients $A^{(m)}(k_1, k_2)$ and $B^{(m)}(k_1, k_2)$, $m = 1, 2$. These equations can be easily solved, and once $A^{(m)}$'s and $B^{(m)}$'s are known, $\mathcal{G}_o^{(m)}$ can be inverted in the (x, y, z) space to give

$$\begin{aligned} G_o^{(1)}(x, y, z) &= -\frac{1}{2\pi}\int_{-\pi}^{\pi}\int_{0}^{\infty} \{2a(a + \gamma b)\, \mathrm{e}^{-kh}\cosh[k(z - \zeta)] \\ &\quad + 2\epsilon ab\, \mathrm{e}^{-kd}\cosh[k(z - \zeta)] - \epsilon b^2\, \mathrm{e}^{k(h-z-\zeta)} + \epsilon a^2\, \mathrm{e}^{-k(h-z-\zeta)} \\ &\quad - b(a + \gamma b)\, \mathrm{e}^{k(d-z-\zeta)} + a(\gamma a + b)\, \mathrm{e}^{-k(d-z-\zeta)}\}\frac{\mathrm{e}^{ik\omega}}{\Delta}\, \mathrm{d}k\, \mathrm{d}\theta, \end{aligned} \tag{18}$$

$$\begin{aligned} G_o^{(2)}(x, y, z) &= \frac{\gamma}{2\pi}\int_{-\pi}^{\pi}\int_{0}^{\infty} \{b(a + b)[\mathrm{e}^{k(h+z-\zeta)} + \mathrm{e}^{k(d-z-\zeta)}] \\ &\quad - a(a + b)[\mathrm{e}^{-k(h+z-\zeta)} + \mathrm{e}^{-k(d-z-\zeta)}]\}\frac{\mathrm{e}^{ik\omega}}{\Delta}\, \mathrm{d}k\, \mathrm{d}\theta, \end{aligned} \tag{19}$$

where $h = h_1 + h_2, \quad d = h_1 - h_2, \quad \epsilon = 1 - \gamma,$
$(a, b) = k \pm k_o \sec^2\theta + i\mu \sec\theta,$
$\omega = (x - \xi)\cos\theta + (y - \eta)\sin\theta,$
$\Delta = 2\epsilon ab \cosh kd + b(\gamma a + b)\, \mathrm{e}^{kh} + a(a + \gamma b)\, \mathrm{e}^{-kh}.$

If we let h_2 in the expressions for $G^{(m)}$ approach infinity, we will recover the Green functions for the case of an infinitely deep lower fluid layer as given in [15]. Also, $G^{(m)}$ can be reduced to the potential of a source moving in a homogeneous fluid of finite-depth, as given in Pond [19], by letting either $\rho_1 = \rho_2$, $\gamma = 0$, or $h_2 = 0$. When $\rho_1 = \rho_2$, Equations (18) and (19) each gives the expression for the single-layer, finite-depth Green function (SLFDGF). However, as $\rho_2 \to \infty$ or $\gamma = \rho_1/\rho_2 = 0$, $G^{(2)}$ becomes identically zero, and $G^{(1)}$ reduces to the SLFDGF. The lower fluid in this case behaves like a solid bottom since its density becomes infinitely large. Lastly, by letting h_2 approach zero in Equation (18), we obtain again the SLFDGF.

3.2. Contour integration in the k-plane

The expressions for $G_o^{(m)}$ in Equations (18) and (19) are real expressions if proper cancellation of the imaginary parts of the integrals are observed. Thus, $G_o^{(m)}$ can be written as

$$G_o^{(m)} = \frac{1}{2\pi} \lim_{\mu \to 0} \Re \left\{ \int_{-\frac{\pi}{2}}^{\frac{\pi}{2}} \int_0^\infty H^{(m)}(k, \theta) \frac{\mathrm{e}^{ik\omega}}{\Delta(k, \theta)}\, \mathrm{d}k\, \mathrm{d}\theta \right\}, \tag{20}$$

where $\Re$ represents the real part of the complex expression inside the braces, and $H^{(m)}(k, \theta)$ are given in Appendix A.

To perform the integration in Equation (20), we first need to locate the poles of the integrand. Let $\kappa = k + i\mu \sec\theta$, $t_n = \tanh kh_n$, $n = 1, 2$, then we can rewrite $\Delta(k, \theta)$ as

$$\begin{aligned} \Delta \;=\; & 4(\cosh kh_1 \cosh kh_2 + \gamma \sinh kh_1 \sinh kh_2) \times \\ & [\kappa - \tfrac{1}{2}k_o \sec^2\theta \Omega_1(k)][\kappa - \tfrac{1}{2}k_o \sec^2\theta \Omega_2(k)], \end{aligned} \tag{21}$$

where

$$\Omega_n(k) = \frac{t_1 + t_2}{1 + \gamma t_1 t_2} \left[1 + (-1)^{n+1} \sqrt{1 - 4(1 - \gamma) \frac{t_1 t_2 (1 + \gamma t_1 t_2)}{(t_1 + t_2)^2}} \right], \tag{22}$$

for $n = 1, 2$. Thus, for a given θ, the roots of Equation (21) are given implicitly by

$$k_n = \tfrac{1}{2}k_o \sec^2\theta \Omega_n(k_n) - i\mu \sec\theta, \quad n = 1, 2. \tag{23}$$

Both k_n are in the lower half of the complex plane, and as μ approaches zero, these poles will approach the positive real axis from below.

With the location of the poles known, we can evaluate the inner integral of Equation (20) using contour integration. Figure 2 shows the appropriate contours for $\omega > 0$ and $\omega < 0$, with Γ_3 and Γ_5 at 45° to the real axis. When $\omega > 0$, the poles k_n are outside the chosen contour, and an application of the residue theorem yields the following equation as $R \to \infty$:

$$\int_0^\infty H^{(m)}(k, \theta) \frac{\mathrm{e}^{ik\omega}\, \mathrm{d}k}{\Delta(k, \theta)} = \int_0^\infty (1 + i) H^{(m)}[u(1 + i), \theta] \frac{\mathrm{e}^{-u\omega}\, \mathrm{e}^{iu\omega}\, \mathrm{d}u}{\Delta[u(1 + i), \theta]}. \tag{24}$$

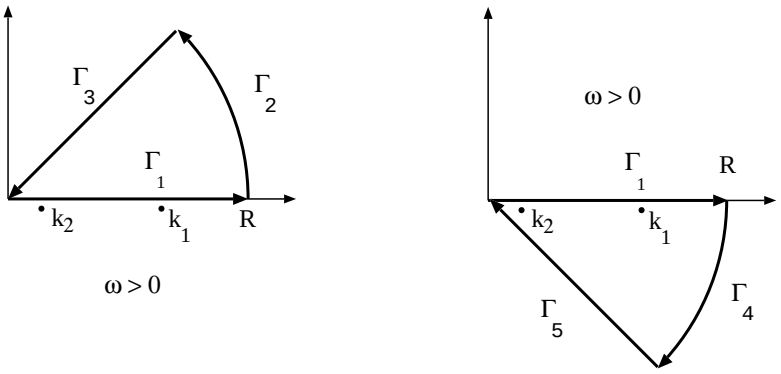

Figure 2. Integration contour in the complex k-plane.

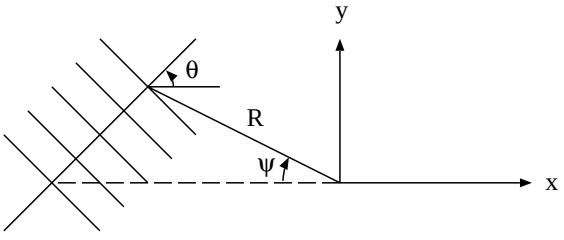

Figure 3. Polar coordinates for a field point.

When $\omega < 0$, the poles k_n are inside the contour, and the residue theorem yields the additional terms from the residues at these poles.

$$\int_0^\infty H^{(m)}(k,\theta)\frac{\mathrm{e}^{ik\omega}\,\mathrm{d}k}{\Delta(k,\theta)} = \int_0^\infty (1-i)H^{(m)}[u(1-i),\theta]\frac{\mathrm{e}^{-u|\omega|}\,\mathrm{e}^{-iu|\omega|}\,\mathrm{d}u}{\Delta[u(1-i),\theta]} - 2\pi i\sum_{n=1}^{2} H^{(m)}(k_n,\theta)\frac{\mathrm{e}^{ik_n\omega}}{\Delta'(k_n,\theta)}, \tag{25}$$

where $\Delta'(k_n,\theta) = \partial\Delta/\partial k|_{k=k_n}$. Note that the integral on the right-hand side of Equation (25) is the complex conjugate of the corresponding integral in Equation (24).

Let us introduce the polar coordinates (r,ψ) as shown in Figure 3. Then $\omega = -r\cos(\theta+\psi)$. Here, θ can be interpreted physically as the orientation of an elemental wave relative to the x-axis, and ψ is the polar angle of (x, y) relative to the negative x-axis. If we further restrict $y \geqslant 0$, then it is easy to see that ω is negative when $-\frac{\pi}{2} < \theta < (\frac{\pi}{2}-\psi)$ and positive when $(\frac{\pi}{2}-\psi) < \theta < \frac{\pi}{2}$. Using these results and Equations (24) and (25), we can write (20), in the limit as $\mu \to 0$, as

$$G_o^{(m)} = \frac{1}{2\pi}\int_{-\frac{\pi}{2}}^{\frac{\pi}{2}}\int_0^\infty \frac{\mathcal{R}\Psi_1^{(m)} + \mathcal{I}\Psi_2^{(m)}}{\mathcal{R}^2+\mathcal{I}^2}\,\mathrm{d}u\,\mathrm{d}\theta + \sum_{n=1}^{2}\Im\left\{\int_{-\frac{\pi}{2}}^{\frac{\pi}{2}-\psi} H^{(m)}(k_n,\theta)\frac{\mathrm{e}^{ik_n\omega}}{\Delta'(k_n,\theta)}\,\mathrm{d}\theta\right\}, \tag{26}$$

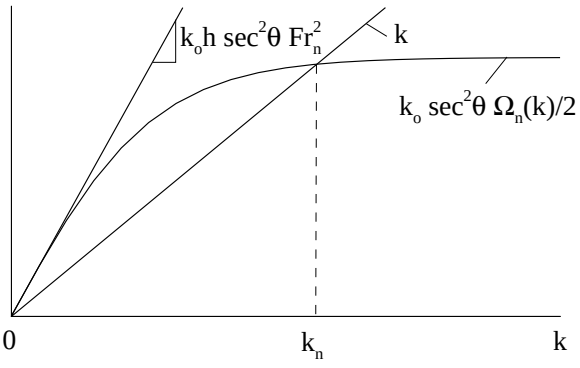

Figure 4. Solution of the wavenumber k_n.

where $\mathcal{R}(u,\theta)$, $\mathcal{S}(u,\theta)$, $\Psi_1^{(m)}(u,\theta)$, $\Psi_2^{(m)}(u,\theta)$, $H^{(m)}(k,\theta)$, and $\Delta'(k,\theta)$ are given in Appendix A. The double integral in this equation contains no singularity and is relatively straightforward to evaluate. The single integrals require the values of k_n and merit additional considerations. As $\mu \to 0$, the poles k_n can be obtained from (23) as

$$k_n = \tfrac{1}{2} k_o \sec^2\theta \Omega_n(k_n), \quad n = 1, 2. \tag{27}$$

The solution of this equation is illustrated in Figure 4, where the expression on the right-hand side is plotted against the variable k. The intersection of this curve with the straight line $f(k) = k$ determines the location of the pole k_n. The slope of this curve at $k = 0$ is given by $k_o h \sec^2\theta \, \mathrm{Fr}_n^2$, where $\mathrm{Fr}_n^2 = \frac{1}{2h} \frac{\partial \Omega_n}{\partial k}\big|_{k=0}$. The nondimensional parameter Fr_n is the critical Froude number corresponding to the wave mode n. Performing the differentiation, we can relate Fr_n to the other physical parameters of the problem as follows:

$$\mathrm{Fr}_n^2 = \tfrac{1}{2} + (-1)^{n+1} \sqrt{\frac{1}{4} - \frac{(1-\gamma) h_1 h_2}{h^2}}. \tag{28}$$

It is easy to see from Figure 4 that the existence of k_n depends on the value of the slope $k_o h \sec^2\theta \, \mathrm{Fr}_n^2$, where k_n exists if this slope is greater than unity. If we define the total depth Froude number as $\mathrm{Fr}^2 = U^2/gh$, then $k_o h \sec^2\theta \, \mathrm{Fr}_n^2 = (\sec\theta \frac{\mathrm{Fr}_n}{\mathrm{Fr}})^2$, and k_n exists if $(\sec\theta \frac{\mathrm{Fr}_n}{\mathrm{Fr}})^2 > 1$. Thus, we can rephrase the criteria for the existence of k_n in terms of the relative values of Fr and Fr_n as follows. If Fr$<$ Fr_n, then k_n exists for all values of θ within the range of integration since $\sec^2\theta \geqslant 1$. If Fr$>$ Fr_n, then k_n exists only if $\sec^2\theta \geqslant \frac{\mathrm{Fr}^2}{\mathrm{Fr}_n^2}$ or for values of θ such that $|\theta| \geqslant \theta_n = \cos^{-1}(\frac{\mathrm{Fr}_n}{\mathrm{Fr}})$. Thus, when Fr$>$ Fr_n, the range of integration of the corresponding single integral in (26) should be modified to exclude the values of θ for which k_n does not exist, *i.e.*, $|\theta| < \theta_n$.

3.3. PHYSICAL INTERPRETATION OF Fr_n

The physical meaning of the critical Froude number Fr_n can be seen by considering waves propagating along the track of the source. We can obtain the wave number for these waves k_n^*

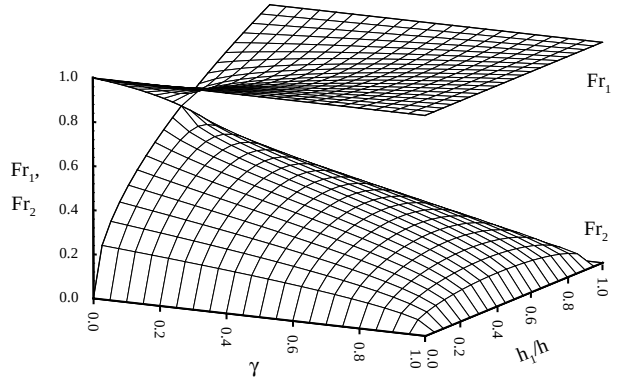

Figure 5. Critical Froude numbers, Fr_1 and Fr_2.

by substituting $\theta = 0$ into (27). Since the phase speed of these waves is equal to the source speed U, the following relationship between phase speed and wave number can be obtained:

$$c_n^2 = \frac{g}{2} \cdot \frac{\Omega_n(k_n^*)}{k_n^*}. \tag{29}$$

As γ approaches unity, this relationship reduces to

$$c_1^2 = \frac{g}{k_1} \tanh k_1 h \quad \text{and} \quad c_2^2 = 0. \tag{30}$$

Thus, c_1 is just the phase speed for surface waves in uniform water of finite depth h. Also, as h_2 approaches infinity, Equation (29) becomes

$$c_1^2 = \frac{g}{k_1} \quad \text{and} \quad c_2^2 = \frac{g}{k_2} \cdot \frac{(1-\gamma)\tanh k_2 h_1}{1 + \gamma \tanh k_2 h_1}. \tag{31}$$

Here, the expression for c_1 is the same as the phase-speed relationship for surface waves in uniform water of infinite depth, and the expression for c_2 is the phase-speed relationship for internal waves for the special case of an infinitely deep lower fluid [15]. In light of these results, we shall now denote waves associated with wave number k_1 as being generated by the surface-wave mode and those associated with wave number k_2 as being generated by the internal-wave mode.

From (29), we can show that the fastest waves are those with the longest wavelengths, and by allowing k_n^* go to zero, we obtain the maximum phase speed for waves of each wave mode. For small k, $\Omega_n(k) \approx \frac{\partial \Omega_n}{\partial k}\big|_{k=0} \cdot k$, and the maximum phase speed is

$$c_{n,M}^2 = \frac{g}{2} \cdot \left.\frac{\partial \Omega_n}{\partial k}\right|_{k=0} = gh\mathrm{Fr}_n^2. \tag{32}$$

Thus, in summary, the critical Froude number Fr_n is the Froude number associated with the fastest wave of wave mode n. This Froude number plays an important role in determining the

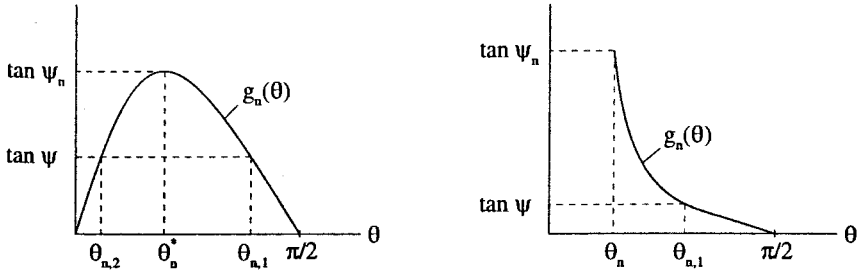

Figure 6. Function $g_n(\theta)$ for $\theta > 0$, case of Fr< Fr_n (left) and Fr> Fr_n (right).

shape of the wave pattern. If we express h_2/h as $1 - h_1/h$, then from (28), Fr_n is a function of the density ratio γ and the depth ratio h_1/h. Figure 5 plots both Fr_1 and Fr_2 for γ and h_1/h from 0 to 1. As can be seen in this figure, Fr_1 is larger than Fr_2. Thus, the maximum phase speed of waves of the surface-wave mode is larger than that of the internal-wave mode.

4. Surface-wave and internal-wave patterns

From the dynamic boundary conditions on the free surface and interface, the surface wave and internal wave patterns due to the motion of a point source can now be expressed as follows:

$$\zeta^{(1)}(x, y) = \frac{U}{g} G_x^{(1)}\Big|_{z=h_1}, \qquad \zeta^{(2)}(x, y) = \frac{U}{\epsilon g}(G_x^{(2)} - \gamma G_x^{(1)})\Big|_{z=0}. \tag{33}$$

To gain more insights into the generated wave patterns, we apply the method of stationary phase to the above equations. Since we are interested in the far field behind the source, we will focus only on the single-integral terms of $G^{(m)}$. Thus, by Equation (26), in the far field $\zeta^{(m)}$ can be expressed as

$$\zeta^{(m)} \sim \sum_{n=1}^{2} \Re\left\{ \int_{-\frac{\pi}{2}}^{\frac{\pi}{2}-\psi} P^{(m)}(k_n, \theta)\, \mathrm{e}^{i(\frac{r}{h}) f_n(\theta,\psi)}\, \mathrm{d}\theta \right\}, \quad r/h >> 1, \tag{34}$$

where $f_n(\theta, \psi) = -hk_n \cos(\theta + \psi)$, $P^{(1)} = [Uk_n \cos\theta \; H^{(1)}/(g\Delta')]|_{z=h_1}$ and $P^{(2)} = [Uk_n \cos\theta \; (H^{(2)} - \gamma H^{(1)})/(\epsilon g \Delta')]|_{z=0}$. Note that each wave pattern $\zeta^{(m)}$ contains contributions from both the surface-wave mode associated with the pole k_1 and the internal-wave mode associated with k_2.

4.1. Stationary points

The stationary points of $f_n(\theta, \psi)$ in (34) for large r/h are the solutions of the following equation [20]:

$$\tan\psi = g_n(\theta) = \frac{\frac{\partial k_n}{\partial\theta} - k_n \tan\theta}{\frac{\partial k_n}{\partial\theta}\tan\theta + k_n}. \tag{35}$$

Since $k_n(\theta)$ is defined for $-\frac{\pi}{2} < \theta < \frac{\pi}{2}$ when Fr< Fr_n, but when Fr> Fr_n, k_n exists only for $\theta_n \leqslant |\theta| < \frac{\pi}{2}$, we need to consider $g_n(\theta)$ for these two cases separately. For positive ψ,

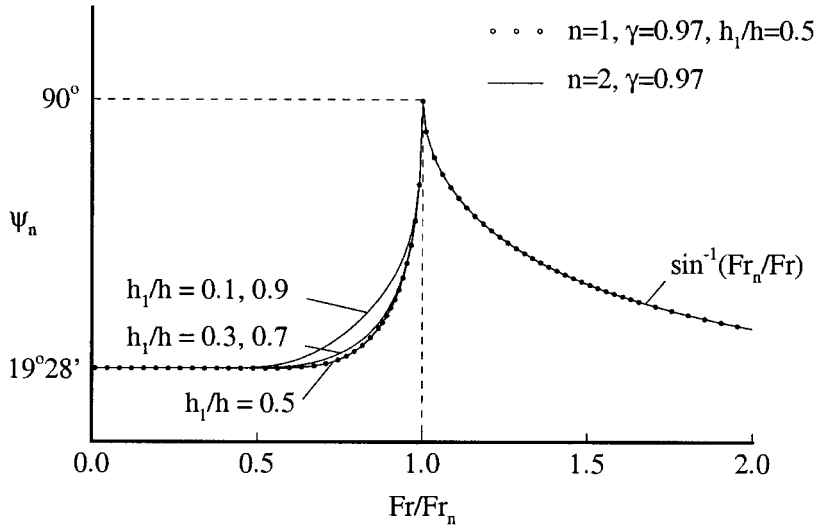

Figure 7. Effects of h_1/h on half-wedge angle ψ_n.

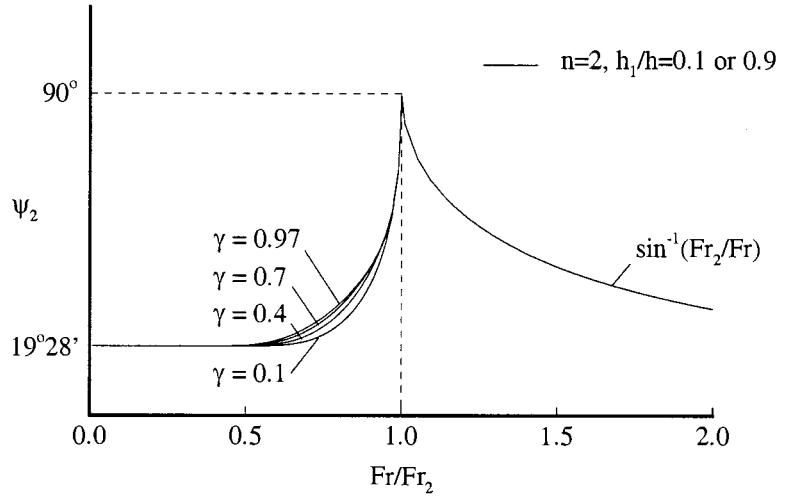

Figure 8. Effects of γ on half-wedge angle ψ_2.

we need only consider positive range of θ. Figure 6 illustrates the general behavior of $g_n(\theta)$ for the subcritical case and supercritical case. It is evident from this figure that stationary points exist only when $\psi < \psi_n$, the maximum half angle in the wake where dominant waves exist. ψ_n is given by $\tan^{-1}[g_n(\theta_n^*)]$. For Fr$>$ Fr$_n$, ψ_n can be shown to be given explicitly by $\sin^{-1}(\mathrm{Fr}_n/\mathrm{Fr})$. For any point (r, ψ) in the wake, either two stationary points $\theta_{n,1}, \theta_{n,2}$ exist for the case of Fr$<$ Fr$_n$, or one stationary point $\theta_{n,1}$ exists for Fr$>$ Fr$_n$. Waves oriented at θ in the range of $[\theta_n, \frac{\pi}{2}]$ represent the divergent wave field, while those in $[0, \theta_n]$, if exist, represent the transverse wave system. Note that in this context, there is considerable analogy to the classical Kelvin wave system. It is helpful to denote the number of stationary points of $f_n(\theta, \psi)$ as s_n, then $s_n = 2$ for Fr$<$ Fr$_n$ and $s_n = 1$ for Fr$>$ Fr$_n$.

Figures 7 and 8 illustrate the dependence of the half-angle ψ_n on h_1/h, γ, and Fr. As the ratio Fr/Fr$_n$ goes from zero to unity, ψ_n increases from $19°28'$, the well-known Kelvin-wave

wake in deep water, to 90°. When $\mathrm{Fr}/\mathrm{Fr}_n > 1$, ψ_n decays as $\sin^{-1}(\mathrm{Fr}_n/\mathrm{Fr})$. The curve ψ_1 versus $\mathrm{Fr}/\mathrm{Fr}_1$ has a very weak dependence on h_1/h and γ. Thus, for a constant Fr, h_1/h and γ affect ψ_1 mainly through the critical Froude number Fr_1. The half-angle ψ_2, on the other hand, shows a stronger dependence on both h_1/h and γ. Figure 7 plots ψ_n against $\mathrm{Fr}/\mathrm{Fr}_n$ for different values of h_1/h but with constant $\gamma = 0{\cdot}97$, the standard fresh water/salt water ratio. The curve ψ_1 is represented here by the dot symbol and is shown only for $h_1/h = 0{\cdot}5$ since ψ_1 is fundamentally the same for other values of h_1/h. The angle ψ_2 is represented by the solid line and is shown for $h_1/h = 0{\cdot}1$, $0{\cdot}3$, $0{\cdot}5$, $0{\cdot}7$ and $0{\cdot}9$. Since the function $g_n(\theta)$ depends only on the product of h_1/h and h_2/h, the half-angle ψ_n is the same for $h_1/h = 0{\cdot}1$, $h_2/h = 0{\cdot}9$ and for $h_1/h = 0{\cdot}9$, $h_2/h = 0{\cdot}1$. Similarly, the curves for $h_1/h = 0{\cdot}3$ and $h_1/h = 0{\cdot}7$ are the same. For $h_1/h = 0{\cdot}5$, the curves for ψ_1 and ψ_2 are practically the same, but as h_1/h moves away from 0.5, ψ_2 increases noticeably for $0{\cdot}5 < \mathrm{Fr}/\mathrm{Fr}_2 < 1$. Figure 8 shows the effects of γ on ψ_2 for constant $h_1/h = 0{\cdot}1$ or $0{\cdot}9$. As γ increases, ψ_2 also increases for a certain range of Fr_2.

4.2. Crestline patterns

For large r/h, Equation (34) has the following expansion

$$\zeta^{(m)}(r,\psi) \sim \sum_{n=1}^{2}\sum_{l=1}^{s_n} A_{n,l}^{(m)}(r,\psi)\cos\left[\left(\frac{r}{h}\right) f_n(\theta_{n,l},\psi) + (-1)^{l+1}\frac{\pi}{4}\right], \tag{36}$$

where

$$A_{n,l}^{(m)}(r,\psi) = P^{(m)}[k_n(\theta_{n,l}),\theta_{n,l}]\sqrt{\frac{2\pi}{(\frac{r}{h})|f_n''(\theta_{n,l},\psi)|}} \tag{37}$$

and $f_n'' = \partial^2 f_n/\partial\theta^2$. According to (36), the surface wave elevation $\zeta^{(1)}$ and the internal wave elevation $\zeta^{(2)}$ can each be composed of up to four different wave systems: the divergent waves ($l = 1$) and the transverse waves ($l = 2$) due to the surface wave mode ($n = 1$), and the divergent and transverse waves due to the internal wave mode ($n = 2$).

The pattern of the crestlines of the divergent and transverse waves can be obtained by a procedure as described in Wehausen and Laitone [21]. These crestlines are determined from the equation of constant phase:

$$-\frac{r}{h}f_n(\theta_{n,l},\psi) + (-1)^l\frac{\pi}{4} = \begin{cases} 2j\pi & \text{for } A^{(m)} > 0, \\ (2j+1)\pi & \text{for } A^{(m)} < 0, \end{cases} \tag{38}$$

where $j = 0, 1, 2, \ldots$. The sign of $A_{n,l}^{(m)}$ depends only on m and n, but not on l. For the surface wave mode, $n = 1$, both $A_{1,l}^{(1)}$, $A_{1,l}^{(2)} \leqslant 0$, and the crestline pattern due to this mode is the

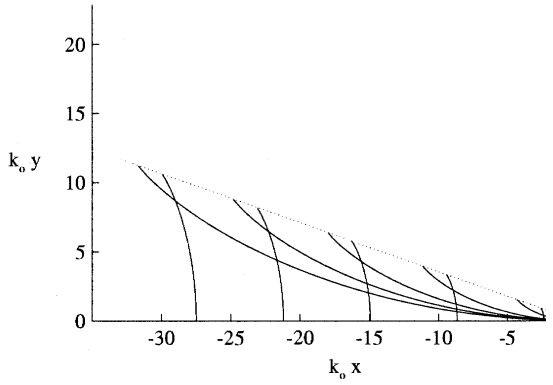

Figure 9. Crestlines of surface wave mode, Fr=0·37, $h_1/h = 0{\cdot}5$, $\gamma = 0{\cdot}5$.

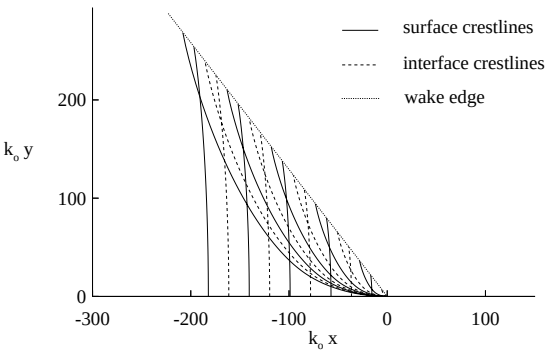

Figure 12. Crestlines of internal wave mode, Fr=0·37, $h_1 h = 0{\cdot}5$, $\gamma = 0{\cdot}5$.

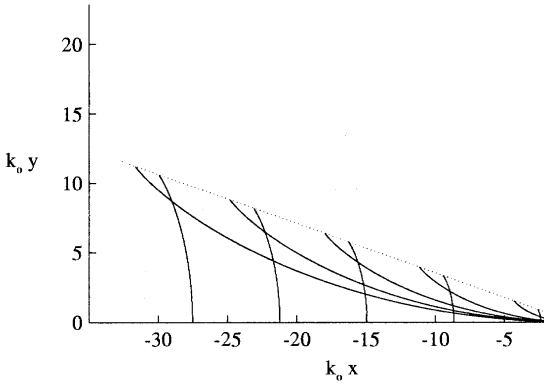

Figure 10. Crestlines of surface wave mode, Fr=0·5, $h_1/h = 0{\cdot}5$, $\gamma = 0{\cdot}5$,

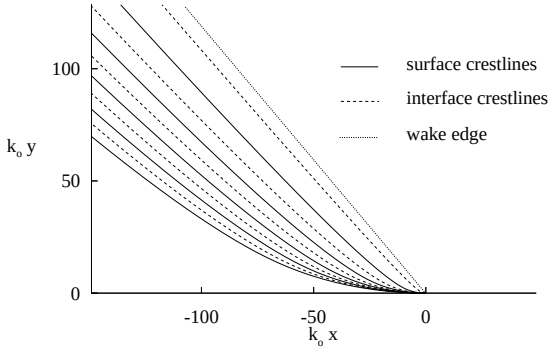

Figure 13. Crestlines of internal wave mode, Fr=0·5, $h_1/h = 0{\cdot}5$, $\gamma = 0{\cdot}5$.

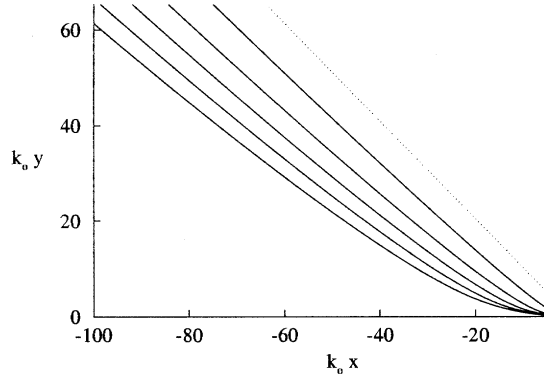

Figure 11. Crestlines of internal wave mode, Fr=1·3, $h_1/h = 0{\cdot}5$, $\gamma = 0{\cdot}5$.

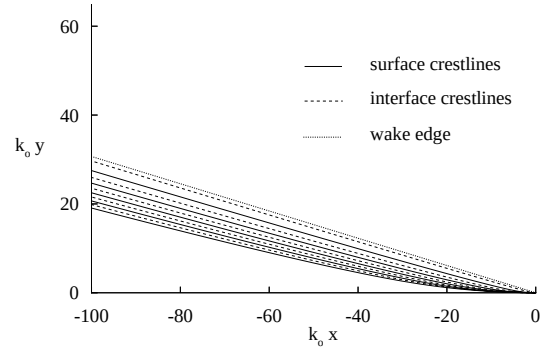

Figure 14. Crestlines of internal wave mode, Fr=1·3, $h_1/h = 0{\cdot}5$, $\gamma = 0{\cdot}5$.

same on the free surface as on the interface. For the internal wave mode, $n = 2$, $A_{2,l}^{(1)} \leqslant 0$, but $A_{2,l}^{(2)} \geqslant 0$, and the crestline pattern on the free surface is 180° out of phase with that on

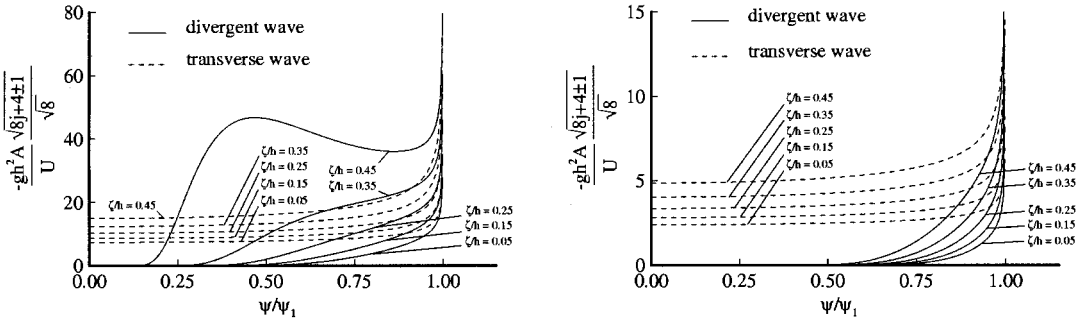

Figure 15. Amplitude functions for surface-wave mode, $\mathrm{Fr}/\mathrm{Fr}_1=0{\cdot}7$, $h_1/h=0{\cdot}5$, $\gamma=0{\cdot}97$; $\bar{A}^{(1)}_{1,l}$ (surface waves, left), $\bar{A}^{(2)}_{1,l}$ (internal waves, right).

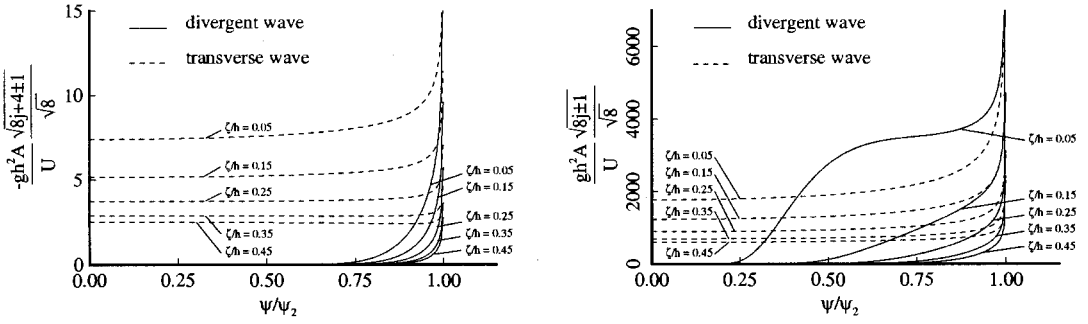

Figure 16. Amplitude functions for internal-wave mode, $\mathrm{Fr}/\mathrm{Fr}_2=0{\cdot}7$, $h_1/h=0{\cdot}5$, $\gamma=0{\cdot}97$; $\bar{A}^{(1)}_{2,l}$ (surface waves, left), $\bar{A}^{(2)}_{2,l}$ (internal waves, right).

the interface, *i.e.*, the crestlines on the free surface are directly above the troughlines on the interface.

Figures 9–11 show the crestlines on the free surface and the interface due to the surface-wave mode for Fr=0·37, 0·5, and 1·3, respectively. In these figures, the depths of the fluid layers are $h_1/h = h_2/h = 0{\cdot}5$, and the density ratio is $\gamma = 0{\cdot}5$. For the above physical parameters, the critical Froude numbers Fr_1 and Fr_2 are 0·924 and 0·383, respectively. Thus, the patterns in Figures 9 and 10 represent the subcritical case and contain both divergent and transverse crestlines, whereas the pattern in Figure 11 corresponds to the supercritical case and contains only divergent crestlines. Figures 12–14 show the crestline patterns due to the internal-wave mode for the same Froude numbers and physical parameters. Here, the crestlines on the free surface, indicated by the solid lines, are different from those on the interface, indicated by the dashed lines. Again, the pattern for the subcritical speed, Figure 12, contains both divergent and transverse crestlines, and the patterns for supercritical speeds, Figures 13 and 14, contain only divergent crestlines.

4.3. Wave amplitude along crestlines

Next, we investigate the behavior of the amplitude function $A^{(m)}_{n,l}$. Nondimensionally, this function will depend on the parameters ζ/h, h_1/h (or h_2/h), γ, and Fr. To understand the dependence of $A^{(m)}_{n,l}$ on these parameters, we will plot $A^{(m)}_{n,l}$ along the crestlines of the divergent and transverse waves ($l = 1, 2$) for mode index $n = 1, 2$. To simplify the plotting, we will

introduce below the nondimensional amplitude function $\bar{A}_{n,l}^{(m)}$ which only depends on ψ and not on r/h. Note that along each crestline the phase is constant, and this allows us to define r/h along the jth crestline in terms of ψ. Thus, if $A_{n,l}^{(m)} > 0$, then $\frac{r}{h} = \frac{-[8j+(-1)^{l+1}]\pi}{4f_n(\theta_{n,l},\psi)}$, and if $A_{n,l}^{(m)} < 0$, then $\frac{r}{h} = \frac{-[8j+4+(-1)^{l+1}]\pi}{4f_n(\theta_{n,l},\psi)}$. Substituting these expressions for r/h in (37) and after some rearrangings, we obtain the following equation for $\bar{A}_{n,l}^{(m)}$:

$$\begin{aligned}\bar{A}_{n,l}^{(m)} &= \frac{gh^2|A_{n,l}^{(m)}|}{U}\frac{\sqrt{8j+c+(-1)^{l+1}}}{\sqrt{8}} \\ &= |\bar{P}^{(m)}[k_n(\theta_{n,l}),\theta_{n,l}]|\sqrt{\frac{-f_n(\theta_{n,l},\psi)}{|f_n''(\theta_{n,l},\psi)|}},\end{aligned} \tag{39}$$

where $c = 0$ for $A_{n,l}^{(m)} > 0$, and $c = 4$ for $A_{n,l}^{(m)} < 0$, $\bar{P}^{(m)}[k_n(\theta_{n,l}),\theta_{n,l}] \equiv gh^2 P^{(m)}[k_n(\theta_{n,l}),\theta_{n,l}]/U$, which is nondimensional. Note that $\bar{A}_{n,l}^{(m)}$ as defined is nonnegative and only a function of ψ.

Effects of ζ/h: Figures 15–16 show the effects of the source vertical location ζ/h on the nondimensionalized amplitude function $\bar{A}_{n,l}^{(m)}$. In these figures, $\gamma = 0.97$, $h_1/h = 0.5$, $\mathrm{Fr}/\mathrm{Fr}_n = 0.7$, and the angle ψ is normalized by the half-angle of the wave pattern ψ_n. Figure 15 plots $\bar{A}_{1,l}^{(1)}$ and $\bar{A}_{1,l}^{(2)}$ along the divergent and transverse wave crestlines. These amplitude functions correspond to the surface and internal waves, respectively, due to the surface-wave mode. As ζ/h increases, *i.e.*, as the source moves closer to the free surface, the amplitudes of both transverse and divergent waves increase, and the divergent waves become more dominant. The waves on the free surface are larger than those on the interface for this mode, and the amplitude of the internal waves actually increases as the source moves away from the interface. Figure 16 plots $\bar{A}_{2,l}^{(1)}$ and $\bar{A}_{2,l}^{(2)}$ which are associated with the surface and internal waves, respectively, due to the internal-wave mode. Here, the wave amplitudes increase, with the divergent waves become more dominant, as the source moves closer to the interface. The internal waves are much larger than the surface waves in this case, and it is possible to have large movement of the interface without visible disturbance on the free surface. Also, the amplitude of the surface waves due to the internal-wave mode actually increases as the source moves away from the free surface and closer to the interface.

Effects of speed (Fr): Figures 17–18 show the effects of the Froude number Fr on $\bar{A}_{n,l}^{(m)}$. In these figures, $\gamma = 0{\cdot}97$, $h_1/h = 0{\cdot}5$, and $\zeta/h = 0{\cdot}25$, *i.e.*, the source is equidistant from the free surface and the interface. The Froude number is normalized by the critical Froude number Fr_n and ranges from a subcritical value $\mathrm{Fr}/\mathrm{Fr}_n = 0{\cdot}5$ to a slightly supercritical value $\mathrm{Fr}/\mathrm{Fr}_n = 1{\cdot}3$. Figure 17 shows the amplitude functions $\bar{A}_{1,l}^{(m)}$ associated with the surface-wave mode, and Figure 18 shows the functions $\bar{A}_{2,l}^{(m)}$ associated with the internal-wave mode. For $\bar{A}_{1,l}^{(1)}$ and $\bar{A}_{2,l}^{(2)}$, the amplitude of the transverse waves decreases and the amplitude of the divergent waves increases as $\mathrm{Fr}/\mathrm{Fr}_n$ approaches unity from below. This phenomenon is similar to that of a source in a uniform fluid of finite depth when the Froude number of the source approaches unity. The behavior of the coupling terms $\bar{A}_{1,l}^{(2)}$ and $\bar{A}_{2,l}^{(1)}$, *i.e.*, the amplitude of the internal waves due to the surface-wave mode and the amplitude of the surface waves due to the internal-wave mode, respectively, is more unpredictable. Although the amplitudes of the divergent waves $\bar{A}_{1,1}^{(2)}$ and $\bar{A}_{2,1}^{(1)}$ increase as $\mathrm{Fr}/\mathrm{Fr}_n$ approaches 1 as before, no definitive

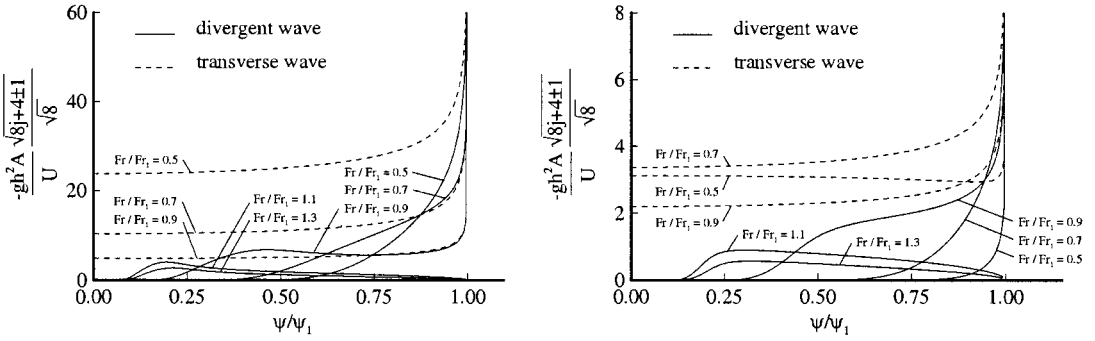

Figure 17. Amplitude functions for surface-wave mode, h_1/h=0·5, ζ/h=0·25, γ=0·97; $\bar{A}^{(1)}_{1,l}$ (surface waves, left), $\bar{A}^{(2)}_{1,l}$ (internal waves, right).

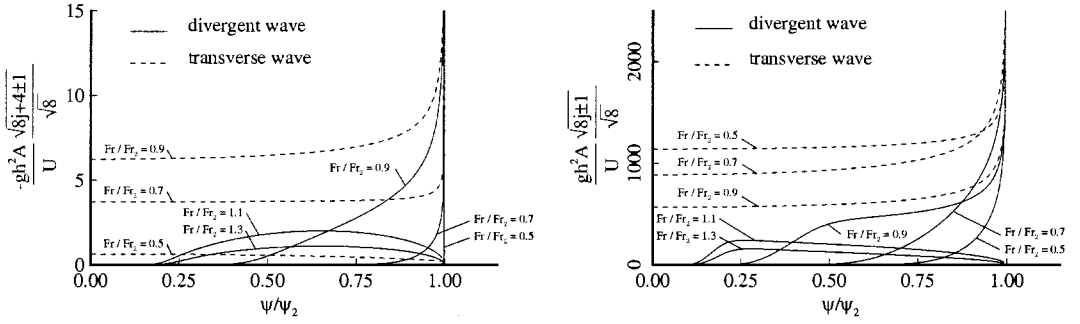

Figure 18. Amplitude functions for internal-wave mode, h_1/h=0·5, ζ/h=0·25, γ=0·97; $\bar{A}^{(1)}_{2,l}$ (surface waves, left), $\bar{A}^{(2)}_{2,l}$ (internal waves, right).

trend can be observed for the amplitude of the transverse waves $\bar{A}^{(2)}_{1,2}$. The amplitude of the transverse waves $\bar{A}^{(1)}_{2,2}$ actually increases as Fr/Fr$_2$ approaches 1. When Fr/Fr$_n$ increases past unity, only divergent waves $\bar{A}^{(m)}_{n,1}$ exist, and their amplitude decreases slowly with increasing Fr/Fr$_n$.

Effects of γ: Figures 19–20 show the effects of γ on $\bar{A}^{(m)}_{n,l}$. In these figures, $h_1/h = 0{\cdot}5$, $\zeta/h = 0{\cdot}25$, and Fr/Fr$_n = 0{\cdot}7$. As shown in Figure 19, the amplitude of the transverse waves $\bar{A}^{(1)}_{1,2}$ increases as γ decreases. This is due to the fact that the lower fluid behaves more like a solid for small γ and, consequently, the effective total depth reduces to a value closer to h_1, and the amplitude of the surface waves due to the surface-wave mode will increase. For the divergent waves $\bar{A}^{(1)}_{1,1}$, the effects of decreasing γ are more complicated. Since Fr/Fr$_1$ is kept fixed, as γ decreases, Fr$_1$ also decreases, and so does Fr. This reduction in Fr causes a more pronounced decrease in the amplitude of the divergent waves than the transverse waves and results in an increase of $\bar{A}^{(1)}_{1,1}$ near the edge of the wake but a decrease in the interior of the wake. Figure 20 plots $\bar{A}^{(2)}_{2,l}$ and shows a large increase in the amplitude of the internal waves as γ becomes closer to unity.

Effects of h_1/h: The effects of h_1/h on $\bar{A}^{(m)}_{n,l}$ are investigated for Fr/Fr$_n = 0{\cdot}7$ and $\gamma = 0{\cdot}7$. The amplitude functions $\bar{A}^{(m)}_{n,l}$ are computed for a source located at a distance of $0{\cdot}01h$ below

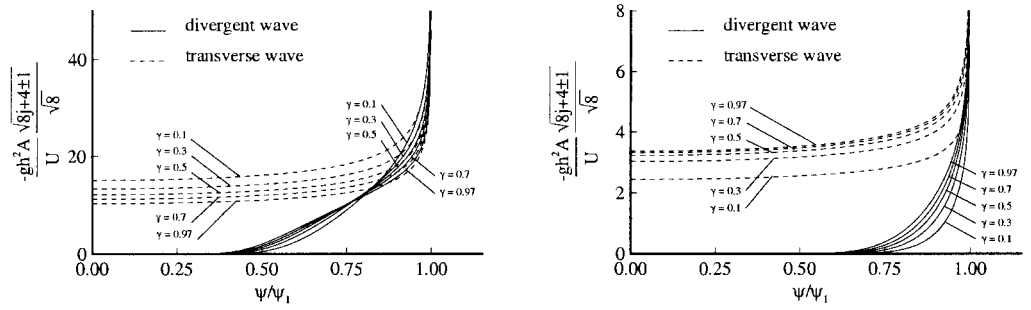

Figure 19. Amplitude functions for surface-wave mode, Fr/Fr$_1$=0·7, h_1/h=0·5, ζ/h=0·25; $\bar{A}^{(1)}_{1,l}$ (surface waves, left), $\bar{A}^{(2)}_{1,l}$ (internal waves, right).

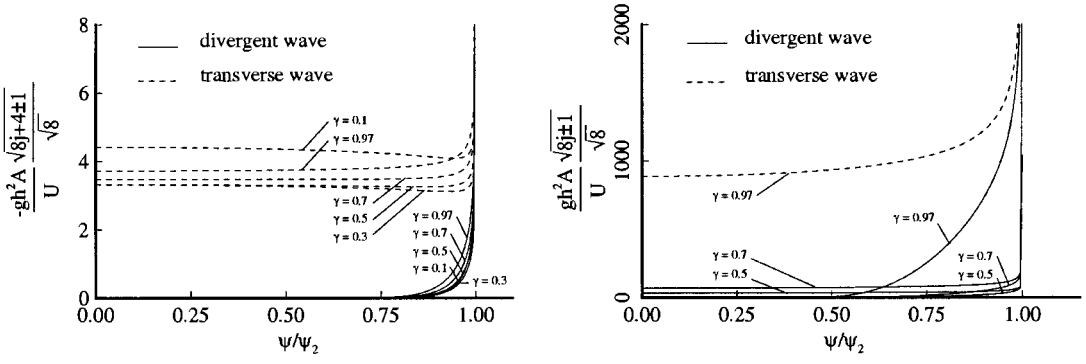

Figure 20. Amplitude functions for internal-wave mode, Fr/Fr$_2$=0·7, h_1/h=0·5, ζ/h=0·25; $\bar{A}^{(1)}_{2,l}$ (surface waves, left), $\bar{A}^{(2)}_{2,l}$ (internal waves, right).

the free surface. The plots of $\bar{A}^{(m)}_{n,l}$ are not presented here because of space limitation. For these parameters, the depth ratio h_1/h has a relatively minor effect on $\bar{A}^{(1)}_{1,l}$. As h_1/h increases, the interface is farther away from the source, and $\bar{A}^{(2)}_{1,l}$ decreases accordingly as expected. Similarly, $\bar{A}^{(m)}_{2,l}$ also decreases as h_1/h increases.

From the results presented so far, one observes that for $\gamma \approx 1$, the coupling terms $\bar{A}^{(2)}_{1,l}$ and $\bar{A}^{(1)}_{2,l}$ are small compared to $\bar{A}^{(1)}_{1,l}$ and $\bar{A}^{(2)}_{2,l}$. However, for γ not close to unity, the coupling terms can be of comparable magnitude as $\bar{A}^{(1)}_{1,l}$ and $\bar{A}^{(2)}_{2,l}$ under certain conditions, in particular, when Fr/Fr$_n \approx 1$ and the source is either close to the free surface or the interface. To illustrate this point, Figure 21 plots $\bar{A}^{(m)}_{n,l}$, $m = 1, 2$ and $n = 1, 2$ for Fr= 0·37, $h_1/h = 0{\cdot}5$, $\zeta/h = 0{\cdot}1$, and $\gamma = 0{\cdot}5$. The critical Froude number Fr$_2$ for this case is 0·383 and Fr/Fr$_2$ = 0·966. In this figure, the surface waves due to the surface-wave mode $\bar{A}^{(1)}_{1,l}$ is of the same order of magnitude as the surface waves due to the internal-wave mode $\bar{A}^{(1)}_{2,l}$. Thus, one can expect interesting surface wave patterns under these conditions.

4.4. WAVE PATTERNS USING FULL EXPRESSIONS OF $G^{(m)}$

The crestline patterns shown in Figures 9–14, as pointed out in Chung and Lim [22], merely express the superposition of the crestlines of the divergent and transverse waves and do not

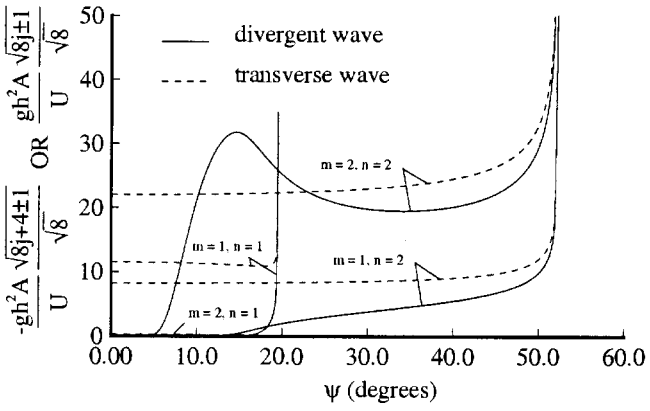

Figure 21. Amplitude functions $\bar{A}_{n,l}^{(m)}$ for Fr $= 0{\cdot}37$, $h_1/h = 0{\cdot}5$, $\zeta/h = 0{\cdot}1$, $\gamma = 0{\cdot}5$.

depend on the amplitudes of these two wave systems. For a better visualization of the surface and internal waves, we proceed to compute $\zeta^{(m)}$ (Equation 33) using the full expressions of $G^{(m)}$ as presented in Equations (7) and (26). An adaptive quadrature using Simpson's rule [23] is used to integrate both the double and single integrals. The poles k_n in the single integrals are obtained by Newton's method. The results of these computations are shown in Figures 22–27 (see also [24] for some preliminary results). In each of these figures, the surface or interface elevations for a square area, $17h \times 17h$ are plotted. The source is located horizontally at $3h$ behind the front edge of the square and vertically in the middle of the upper fluid layer. The depth of each fluid layer is $15m$, and density ratio γ is 0·97 for Figures 22–24 and 0·5 for Figures 25–27. These plots are intended to illustrate the effects of the source speed on the generated surface and internal waves, and also to demonstrate the coupling effects when γ is not close to unity. Since $\mathrm{Fr}_2 < \mathrm{Fr}_1$, it is convenient to classify the wave patterns according to Fr$< \mathrm{Fr}_2$, $\mathrm{Fr}_2 <$ Fr $< \mathrm{Fr}_1$, or $\mathrm{Fr}_1 <$ Fr. Thus, for each value of γ, the wave patterns for Froude numbers in each of the three regimes are shown. In Figures 22–24, $\gamma = 0{\cdot}97$, and $\mathrm{Fr}_1 = 0{\cdot}996$ and $\mathrm{Fr}_2 = 0{\cdot}087$. The three Froude numbers selected for this case are Fr$= 0{\cdot}08$, 0·5, and 1·3. Note that in all these figures, the wave elevations $\zeta^{(m)}$ are magnified for clarity, and the magnification factor is indicated in the caption for each figure.

Figure 22 shows the surface waves and internal waves for Fr$= 0{\cdot}08$. At this low Froude number, the waves due to the surface-wave mode are negligible, but large waves are generated on the interface through the internal-wave mode. Since Fr is less than Fr_2 but very close to it, both divergent and transverse waves are present, and the half-angle of the wave pattern is very close to 90°. The amplitude of the internal waves is approximately 75 times larger than that of the surface waves. The conditions in these two plots correspond to the well-known dead-water phenomenon where a ship is traveling close to the speed of the fastest internal waves and is experiencing a large wave drag due to the generation of large amplitude internal waves. Note also that for $\gamma \approx 1$, it is possible to have large vertical displacement of the interface without significant displacement of the free surface.

Figure 23 plots the surface and internal wave patterns for Fr$= 0{\cdot}5$. At this Froude number, the source is traveling faster than the fastest internal waves and is in the supercritical speed with respect to the internal-wave mode. However, it is still moving at the subcritical speed

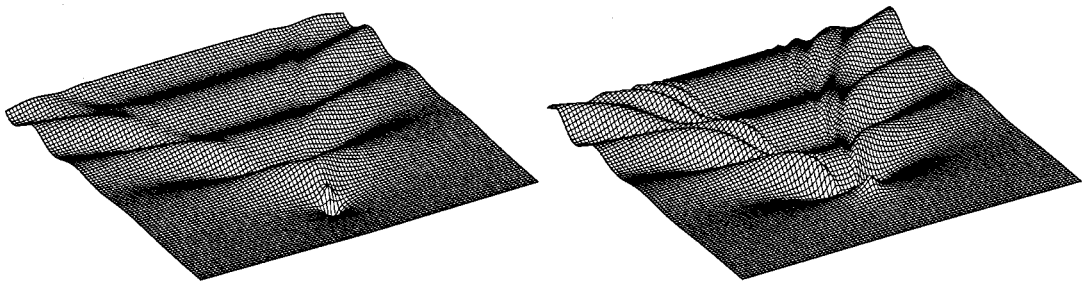

Figure 22. Surface waves (left), $4{\cdot}6E5 \cdot \zeta^{(1)}$ and internal waves (right), $6{\cdot}2E3 \cdot \zeta^{(2)}$ for Fr$=$ 0·08, $h_1/h = 0{\cdot}5$, $\zeta/h = 0{\cdot}25$, $\gamma = 0{\cdot}97$.

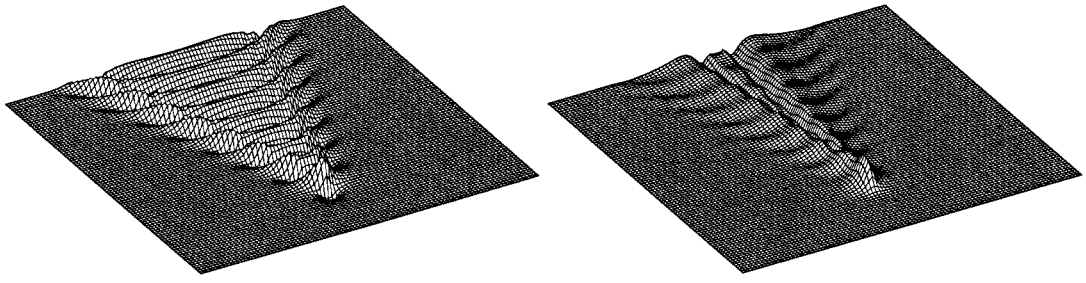

Figure 23. Surface waves (left), $3{\cdot}5E4 \cdot \zeta^{(1)}$ and internal waves (right), $3{\cdot}9E4 \cdot \zeta^{(2)}$ for Fr$=$ 0·5, $h_1/h = 0{\cdot}5$, $\zeta/h = 0{\cdot}25$, $\gamma = 0{\cdot}97$.

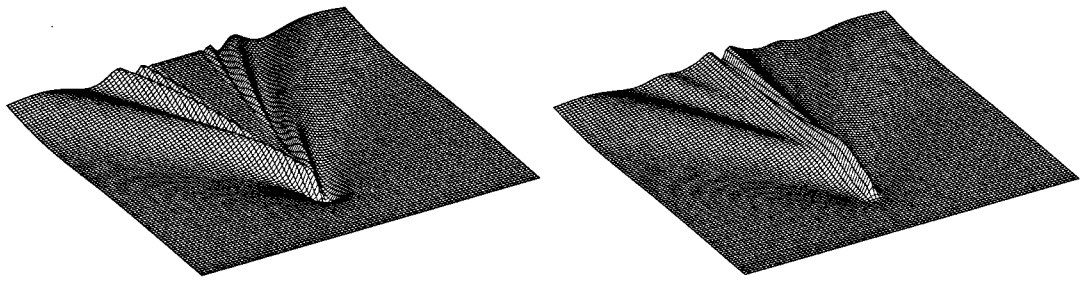

Figure 24. Surface waves (left), $6{\cdot}5E4 \cdot \zeta^{(1)}$ and internal waves (right), $1{\cdot}1E5 \cdot \zeta^{(2)}$ for Fr$=$ 1·3, $h_1/h = 0{\cdot}5$, $\zeta/h = 0{\cdot}25$, $\gamma = 0{\cdot}97$.

with respect to the surface-wave mode. The surface wave pattern is similar to the Kelvin wave pattern, and the influence of the internal-wave mode on the free surface is negligible, *i.e.*, $\bar{A}^{(1)}_{2,l} \ll \bar{A}^{(1)}_{1,l}$. The internal wave pattern contains the narrow V-wake associated with the divergent wave system of the internal-wave mode and also the divergent and transverse waves systems associated with the surface-wave mode.

Figure 24 shows the surface and internal wave pattern for Fr$=$ 1·3. The source, in this case, is travelling faster than the fastest surface and internal waves and is at the supercritical speed with respect to either mode. At this Froude number, the half-angle ψ_2 is much smaller than the half-angle ψ_1, and it is possible to discern the contribution of each mode to the surface and internal waves. Again, the surface wave pattern shows little contribution from the internal-wave mode. The narrow V-wake of the internal-wave mode is not seen on the free surface. Near the source's track, the free surface is practically flat. On the interface, the narrow V-

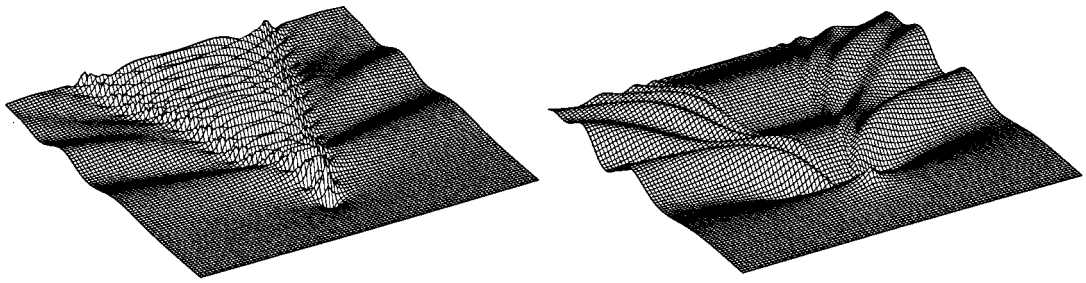

Figure 25. Surface waves (left), $4{\cdot}4E4 \cdot \zeta^{(1)}$ and internal waves (right), $3{\cdot}3E4 \cdot \zeta^{(2)}$ for Fr= 0·37, $h_1/h = 0{\cdot}5$, $\zeta/h = 0{\cdot}25$, $\gamma = 0{\cdot}5$.

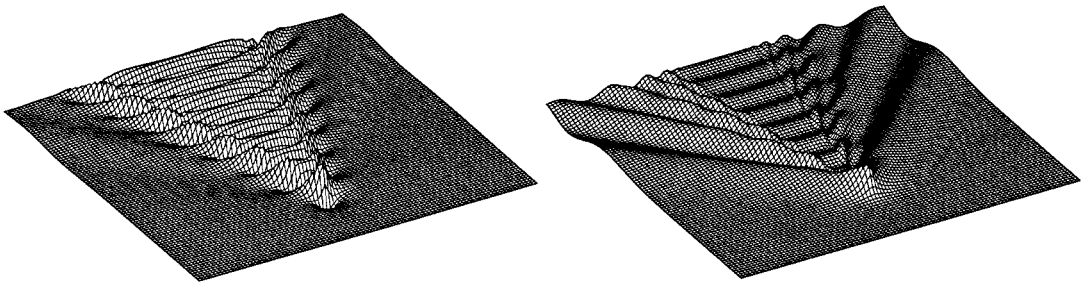

Figure 26. Surface waves (left), $4{\cdot}0E4 \cdot \zeta^{(1)}$ and internal waves (right), $6{\cdot}4E4 \cdot \zeta^{(2)}$ for Fr= 0·5, $h_1/h = 0{\cdot}5$, $\zeta/h = 0{\cdot}25$, $\gamma = 0{\cdot}5$

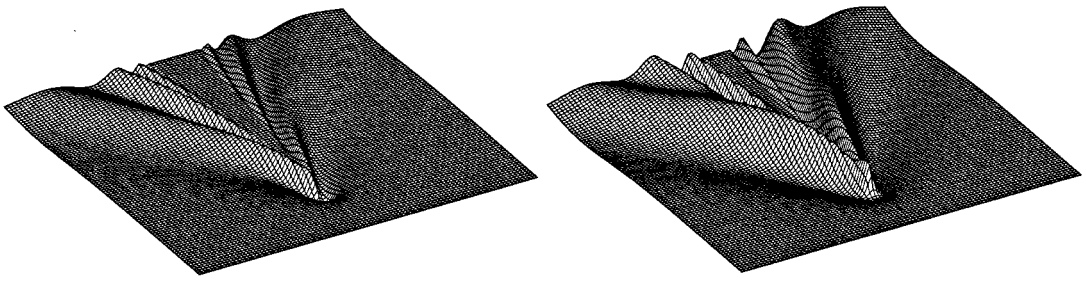

Figure 27. Surface waves (left), $6{\cdot}5E4 \cdot \zeta^{(1)}$ and internal waves (right), $3{\cdot}0E5 \cdot \zeta^{(2)}$ for Fr= 1·3, $h_1/h = 0{\cdot}5$, $\zeta/h = 0{\cdot}25$, $\gamma = 0{\cdot}5$

wake is prominent along with the divergent waves of the surface-wave mode, radiating out at a wider angle from the source's track.

Figures 25–27 show the wave patterns for $\gamma = 0{\cdot}5$. The critical Froude numbers for this case are $\mathrm{Fr}_1 = 0{\cdot}924$ and $\mathrm{Fr}_2 = 0{\cdot}383$, and the Froude numbers chosen to illustrate the three Froude number regimes are 0·37, 0·5, and 1·3. Figure 25 shows the surface and internal waves for Fr= 0·37. The parameters in these figures are similar to those of Figure 21 with the exception of ζ/h. In Figure 21, the source is closer to the interface than in Figure 25. However, the conclusions drawn from Figure 21 are still valid for Figure 25, namely, $\bar{A}^{(1)}_{1,l}$, $\bar{A}^{(1)}_{2,l}$, and $\bar{A}^{(2)}_{2,l}$ are roughly of the same order of magnitude. The surface wave pattern contains

a significant contribution from the internal wave mode whose divergent waves radiate out at a angle almost 90° to the source's track. It also has the usual contribution from the surface-wave mode within a smaller half-angle ψ_1. Figure 25 again confirms what has already been observed in Figure 21, namely, the internal waves due to the surface-wave mode is much smaller than the internal waves due to the internal-wave mode. In Figure 25, one can observe the phase shift in the surface and internal waves due to the internal-wave mode, where the crests of the divergent waves on the free surface is above the troughs of the waves on the interface. One can also observe the longer wavelengths of the internal-wave mode compared to the surface wave-mode.

Figure 26 presents the results for Fr$=$ 0·5. Again, one can see the coupling effects on both the surface and internal waves. The surface waves and the internal waves contain the divergent and transverse waves due to the surface-wave mode and the divergent waves due to the internal-wave mode. Finally, Figure 27 shows the wave patterns for Fr$=$ 1·3. The surface wave pattern is similar to that in Figure 24 for $\gamma = 0{\cdot}97$ where the contribution from the internal-wave mode is negligible. However, the contribution from the surface-wave mode to the internal waves is significant as can be seen in Figure 27.

5. Conclusions

The velocity potentials of a steadily translating source in the upper layer of a two-layer fluid of finite depth is derived in a form amenable to numerical treatment. These velocity potentials consist of a double-integral term which is symmetric with respect to both the x and y-axes, and two single-integral terms associated with the surface-wave mode and internal-wave mode. The velocity potential are then used to analyze the surface and internal wave patterns in the far field of the source using the method of stationary phase. The results are further confirmed and illustrated by numerically evaluating the full expressions of the potentials.

Two critical Froude numbers, Fr_1 and Fr_2, are defined in the derivation which play an important role in determining the shapes of the wave patterns. These critical Froude numbers are the Froude numbers correspond to the fastest waves of each mode, normalized by the total depth. From the asymptotic analysis, it is shown that for the nth wave mode, if the total depth Froude number of the source Fr is less than Fr_n, *i.e.*, the source is moving slower than the fastest waves of the n-mode, then both divergent and transverse waves are generated for that mode. However, when Fr$>$ Fr_n, then only divergent waves are excited for this mode. Further, each wave mode contributes to the surface waves and internal waves. Thus, there are a maximum of four different wave systems: two on the free surface because of the surface and internal wave modes and two on the interface because of these same wave modes. When the density ratio of the two fluid layers, $\gamma = \rho_1/\rho_2$, is close to unity, then $\mathrm{Fr}_1 \approx 1$ and $\mathrm{Fr}_2 \ll 1$. The internal-wave mode in this case is important only if the speed of the source is small and Fr $\approx \mathrm{Fr}_2$. The surface-wave mode, on the other hand, is important when Fr $\gg \mathrm{Fr}_2$. Also in this case, the surface waves associated with the internal-wave mode and the internal waves associated with the surface-wave mode, the 'cross-coupling influence', are normally not very significant. This could allow one to treat the surface waves separately from the internal waves as were done by many authors. However when γ is not close to one, Fr_1 and Fr_2 can be of comparable magnitudes, and in certain range of Froude numbers, both modes become important. Furthermore, the surface and internal waves associated with the 'cross-coupling influence' are significant, and one have to account for all four wave systems.

Appendix A

The functions $\mathcal{R}(u,\theta)$, $\mathcal{S}(u,\theta)$, $\Psi_1^{(m)}(u,\theta)$, $\Psi_2^{(m)}(u,\theta)$, $H^{(m)}(k,\theta)$, and $\Delta'(k,\theta)$ in Equation (26) are given in this Appendix as follows.

$$\begin{aligned}\mathcal{R}(u,\theta) &= \epsilon k_o^2(\cosh uh\cos uh - \cosh ud\cos ud)\\ &\quad -2uk_o\cos^2\theta(\sinh uh\cos uh - \cosh uh\sin uh)\\ &\quad -2u^2\cos^4\theta[(1+\gamma)\sinh uh\sin uh + \epsilon\sinh ud\sin ud],\end{aligned} \tag{40}$$

$$\begin{aligned}\mathcal{S}(u,\theta) &= \epsilon k_o^2(\sinh uh\sin uh - \sinh ud\sin ud)\\ &\quad -2uk_o\cos^2\theta(\cosh uh\sin uh + \sinh uh\cos uh)\\ &\quad +2u^2\cos^4\theta[(1+\gamma)\cosh uh\cos uh + \epsilon\cosh ud\cos ud],\end{aligned} \tag{41}$$

$$\begin{aligned}\Psi_1^{(1)} &= 2u^2\cos^4\theta[\epsilon(M_1+M_2+M_7-M_8-N_1-N_2-N_7+N_8)\\ &\quad +(1+\gamma)(M_3-M_4+M_5+M_6-N_3+N_4-N_5-N_6)]\\ &\quad -4uk_o\cos^2\theta[\gamma(N_3+N_4)+N_5+N_6+\epsilon(N_7+N_8)]\\ &\quad +\epsilon k_o^2(M_1+M_2+M_3-M_4-M_5-M_6-M_7+M_8\\ &\quad +N_1+N_2+N_3-N_4-N_5-N_6-N_7+N_8),\end{aligned} \tag{42}$$

$$\begin{aligned}\Psi_2^{(1)} &= -2u^2\cos^4\theta[\epsilon(M_1+M_2+M_7-M_8+N_1+N_2+N_7-N_8)\\ &\quad +(1+\gamma)(M_3-M_4+M_5+M_6+N_3-N_4+N_5+N_6)]\\ &\quad -4uk_o\cos^2\theta[\gamma(M_3+M_4)+M_5+M_6+\epsilon(M_7+M_8)-4]\\ &\quad +\epsilon k_o^2(M_1+M_2+M_3-M_4-M_5-M_6-M_7+M_8\\ &\quad -N_1-N_2-N_3+N_4+N_5+N_6+N_7-N_8)-16\epsilon uk_o^2h_2,\end{aligned} \tag{43}$$

$$\begin{aligned}\Psi_1^{(2)} &= 4\gamma u^2\cos^4\theta(M_3-M_4+M_6-M_9-N_3+N_4-N_6+N_9)\\ &\quad -4\gamma uk_o\cos^2\theta(N_3+N_4+N_6+N_9),\end{aligned} \tag{44}$$

$$\begin{aligned}\Psi_2^{(2)} &= 4\gamma u^2\cos^4\theta(-M_3+M_4-M_6+M_9-N_3+N_4-N_6+N_9)\\ &\quad -4\gamma uk_o\cos^2\theta(M_3+M_4+M_6+M_9-4),\end{aligned} \tag{45}$$

where

$$M_j = \mathrm{e}^{-u(d_j+|\omega|)}\cos[u(d_j-|\omega|)],\quad N_j = \mathrm{e}^{-u(d_j+|\omega|)}\sin[u(d_j-|\omega|)],$$
$$d_{1,2} = d\mp z\pm\zeta,\qquad d_{3,4} = \pm(d-z-\zeta),$$
$$d_{5,6} = h\mp z\pm\zeta,\qquad d_{7,8} = \pm(h-z-\zeta),$$
$$d_9 = -h-z+\zeta,$$

$$
\begin{aligned}
H^{(1)}(k,\theta) \;=\; & -8kk_o \sec^2\theta\{\epsilon\cosh[k(h-z-\zeta)]+\gamma\cosh[k(d-z-\zeta)]\} \\
& +4\epsilon(k^2+k_o^2\sec^4\theta)\sinh[k(h-z-\zeta)] \\
& +4[(1+\gamma)k^2-\epsilon k_o^2\sec^4\theta]\sinh[k(d-z-\zeta)] \\
& -4\{[(1+\gamma)k^2+2kk_o\sec^2\theta+\epsilon k_o^2\sec^4\theta]\,\mathrm{e}^{-kh} \\
& +\epsilon(k^2-k_o^2\sec^4\theta)\,\mathrm{e}^{-kd}\}\cosh[k(z-\zeta)], \qquad (46)
\end{aligned}
$$

$$
\begin{aligned}
H^{(2)}(k,\theta) \;=\; & 16\gamma\cosh[k(h_2+z)]\cdot \\
& \{k^2\sinh[k(h_1-\zeta)]-kk_o\sec^2\theta\cosh[k(h_1-\zeta)]\}, \qquad (47)
\end{aligned}
$$

$$
\begin{aligned}
\Delta'(k,\theta) \;=\; & 4k[(1+\gamma)-hk_o\sec^2\theta]\cosh kh \\
& +2[(1+\gamma)hk^2-2k_o\sec^2\theta+\epsilon hk_o^2\sec^4\theta]\sinh kh \\
& +4\epsilon k\cosh kd+2\epsilon d(k^2-k_o^2\sec^4\theta)\sinh kd. \qquad (48)
\end{aligned}
$$

Acknowledgements

Research reported in this paper has been supported primarily by the Office of Naval Research under grant N00014-91-J1614 and N00014-95-J-1-0980. Partial support from a grant from the Shell Foundation is also acknowledged.

References

1. V. W. Ekman, On dead water. *Norwegian North Polar Expedition, 1893-1896, Scientific Results* 5 (1904) 1–150.
2. T. Miloh and M. P. Tulin, A theory of dead water phenomena. *Proc. 17th Symp. Naval Hydrodyn.*, The Hague (1988) 127–142.
3. T. Miloh, M. P. Tulin and G. Zilman, Dead-water effects of a ship moving in stratified seas. *J. Offshore Mech. Arctic Eng.* 115 (1993) 105–110.
4. B. A. Hughes, Surface wave wakes and internal wave wakes produced by surface ships. *Proc. 16th Symp. Naval Hydrodyn.*, Berkeley, CA (1986), 1–17.
5. M. P. Tulin and T. Miloh, Ship internal waves in a shallow thermocline: the supersonic case. *Proc. 18th Symp. Naval Hydrodyn.*, Ann Arbor, MI (1991) 567–581.
6. J. B. Keller and W. H. Munk, Internal wave wakes of a body moving in a stratified fluid. *Phys. Fluids* 13 (1970) 1425–1431.
7. C. S. Yih and S. Zhu, Patterns of ship waves. *Q. Appl. Math.* 47 (1989) 17–33.
8. M. P. Tulin, P. Wang and Y. Yao, Numerical prediction of ship generated internal waves in a stratified ocean at supercritical Froude numbers. *Proc. 6th Int. Conf. Num. Ship Hydrodyn.* Iowa City (1993) 519–539.
9. H. L. Wong and S. M. Çalişal, Numerical algorithms for slender bodies with vortex shedding and density stratification. *J. Ship Res.* 40 (1996) 11–21.
10. R. W. Yeung and S. H. Kim, A new development in the theory of oscillating and translating slender ships. *Proc. 15th Symp. Naval Hydrodyn.* Hamburg, W. Germany (1984) 195–212.
11. A. A. Hudimac, Ship waves in a stratified ocean. *J. Fluid Mech.* 11 (1961) 229–243.

12. G. D. Crapper, Ship waves in a stratified ocean. *J. Fluid Mech.* 29 (1967) 667–672.
13. L. N. Sretenskii, On the wave resistance of ships in the presence of internal waves. *Izv. Akad. Nauk C. C. C. R., Otdelenie Tekhnicheskikh* 1 (1959) 56–63.
14. P. N. Uspenskii, On the wave resistance of a ship in the presence of internal waves under conditions of finite depth. *Akad. Nauk USSR Tr. Morskogo Gidrophizicheskogo Instituta* 18 (1959) 68–84.
15. T. Sabunçu, The theoretical wave resistance of a ship travelling under interfacial wave conditions. Trondheim: Norwegian Ship Model Exp. Tank (1961) 124 pp.
16. J. H. Michell, Wave resistance of a ship. *Phil. Mag.* 5, 45 (1898) 106–123.
17. H. Lamb, *Hydrodynamics*. New York: Dover Publication Inc. (1932) 738 pp.
18. I. S. Gradshteyn and I. M. Ryzhik, *Table of Integrals, Series, and Products*. Orlando: Academic Press (1980) 1160 pp.
19. H. L. Pond, The theoretical pressure signature of bodies represented by source distributions. Maryland: DTMB Rep. No. C-743 (1957) 38 pp.
20. E. T. Copson, *Asymptotic Expansions*. Cambridge: Cambridge U. Press (1967) 119 pp.
21. J. V. Wehausen and E. V. Laitone, Surface waves. *Handbuch der Physik* 9 (1960) 446–778.
22. Y. K. Chung and J. S. Lim, A review of the Kelvin ship wave pattern. *J. Ship Res.* 35 (1991) 191–197.
23. S. D. Conte and C. Boor, *Elementary Numerical Analysis*. New York: McGraw-Hill (1980).
24. T.Nguyen and R. W. Yeung, Steady-wave sytems in a two-layer fluid of finite depth. *Proc. 12th Int. Workshop Water Waves and Floating Bodies*. Marseilles, France (1997) 115–119.